Exploring the transition of polydopamine-shelled perfluorohexane emulsion droplets into microbubbles using small- and ultra-small-angle neutron scattering analyses

Journal:	*Physical Chemistry Chemical Physics*
Manuscript ID	CP-ART-03-2021-001146
Article Type:	Paper
Date Submitted by the Author:	15-Mar-2021
Complete List of Authors:	Vidallon, Mark; Monash University, School of Chemistry Giles, Luke; Monash University, School of Chemistry Crawford, Simon; Monash University, Ramaciotti Centre for Cryo-Electron Microscopy, Monash University, Clayton VIC 3800, Australia Bishop, Alexis; Monash University, School of Physics Tabor, Rico; Monash University, School of Chemistry de Campo, Liliana; ANSTO, ACNS Teo, Boon; Monash University, School of Chemistry; Monash University

ARTICLE

Exploring the transition of polydopamine-shelled perfluorohexane emulsion droplets into microbubbles using small- and ultra-small-angle neutron scattering

Received 00th January 20xx,
Accepted 00th January 20xx

DOI: 10.1039/x0xx00000x

Mark Louis P. Vidallon,[a] Luke W. Giles,[a] Simon Crawford,[b] Alexis I. Bishop,[c] Rico F. Tabor,[a] Liliana de Campo,*[d] and Boon Mian Teo*[a]

Perfluorocarbon emulsion droplets are interesting colloidal systems with applications, ranging from diagnostics and theranostics to drug delivery, due to their controllable phase transition into microbubbles via heat application or acoustic droplet vapourisation. This work highlights the application of small- and ultra-small-angle neutron scattering (SANS and USANS, respectively), in combination with contrast variation techniques, in observing the *in situ* phase transition of polydopamine-stabilised, perfluorohexane (PDA/PFH) emulsion droplets into microbubbles during heating. Results show peak USANS intensities at temperatures around 90°C, which indicate that the phase transition of PDA/PFH emulsion droplets occur at significantly higher temperatures than the bulk boiling point of pure liquid PFH (56°C). Analysis and model fitting of the SANS and USANS data allowed us to estimate droplet sizes and interfacial properties at different temperatures (20°C, 90°C, and 20°C after cooling), giving valuable insights about the transformation of these polydisperse, emulsion droplet systems.

1 Introduction

Perfluorocarbon (PFC), phase-transition emulsion droplets are promising materials in the field of biomedicine due to the easily controllable transformation of these liquid droplets into microbubbles using localised heat[1] or via acoustic droplet vapourisation.[2] These materials have are made from small liquid droplets of low-boiling point perfluorocarbon cores, such as perfluorohexane and perfluoropentane,[3] which are stabilised by a shell material, usually made with surfactant molecules (usually phospholipids), proteins, polymers, solid particles, or combinations of these.[4-7] The phase change and formation of microbubbles from the liquid PFC core have vast applications, such as in drug[8] and oxygen delivery,[9] contrast-enhanced ultrasound imaging,[10, 11] sonothrombolysis,[12] and other diagnostic and theranostic applications.

Because of the well-known acoustic droplet vapourisation of phase-transition droplets, the most common characterisation techniques for these systems are ultrasound-related, which include acoustic vapourisation threshold determination and ultrasound imaging.[13] Designs of phase-transition emulsion droplets in the past decade are being improved and innovated through the incorporation of various materials, including polydopamine (PDA),[4, 10] blood cell membranes,[9] and magnetic[2] and plasmonic nanoparticles,[14] that confer advantageous properties and functions, such as multi-responsiveness and surface functionality.[15] With these innovations, new characterisation techniques for these materials are being developed and improved. Heat[16] and optical (laser and near-infrared radiation)[8, 17] triggers for the phase change of these materials are becoming popular in the fields of diagnostics and theranostics, because of the added benefit of using heat to kill bacteria[18] and cancer cells,[10] and trigger other biological responses, and the enhanced photoacoustic response of these materials.[5, 19]

The study of PFC emulsion droplets and their heat-triggered phase change is exciting, but has been very challenging with some conventional imaging and scattering techniques. Optical and electron microscopy (EM) imaging are both powerful tools in visualising PFC droplet and the ensuing microbubbles. However, optical imaging techniques are limited by their resolution[20] and the size and refractive index differences between the emulsion droplets and microbubbles.[2, 21-23] The high vacuum and possibility of electron beam damage,[24] and

---

[a] School of Chemistry, Monash University, Clayton, VIC, Australia 3800
[b] Ramaciotti Centre for Cryo-Electron Microscopy, Monash University, Clayton, VIC, Australia 3800
[c] School of Physics and Astronomy, Monash University, Clayton, VIC, Australia 3800
[d] Australian Nuclear Science and Technology Organisation (ANSTO), New Illawarra Rd, Lucas Heights, NSW, Australia 2234

*Corresponding authors
Boon Mian Teo (boonmteo@gmail.com)
Liliana de Campo (lilianadecampo@ansto.gov.au)

Electronic Supplementary Information (ESI) available: TEM images (Fig. S1); USANS patterns of droplets and bubbles (Fig. S2); 2D USANS patterns of droplets and bubbles (Fig. S3); 2D SANS patterns of droplets (Fig. S4); and power-law exponents from SANS data fitting (Table S1).

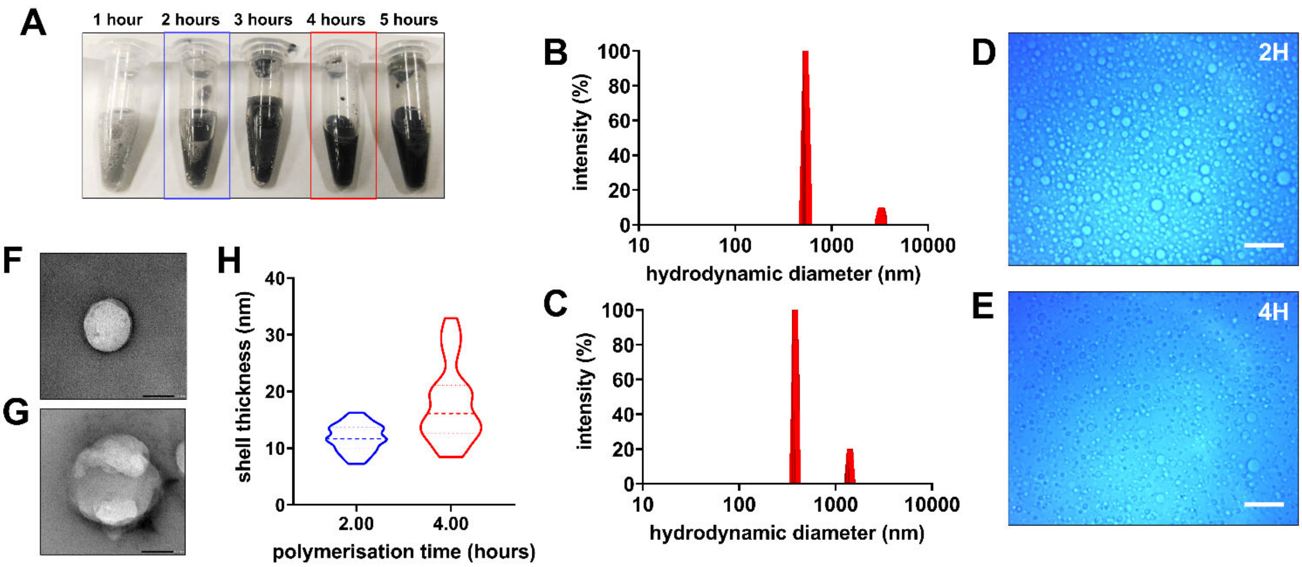

Figure 1. Photographs of concentrated (A) PDA/PFH emulsions with different polymerisation times. Droplet size distributions based on dynamic light scattering analysis of (B) sample 2H and (C) sample 4H. Optical microscopy images of (D) sample 2H and (E) sample 4H. Representative transmission electron micrographs of (F) sample 2H and (G) sample 4H. Violin plots showing the differences in the shell thicknesses of sample 2H and sample 4H. Scale bars = (D and E) 10 µm, (F and G) 100 nm.

limitations in applying various stimuli to induce phase change limit the application of EM imaging in observing real-time phase. Dynamic light scattering (DLS) is another classical but powerful colloidal characterisation method; however, the substantial differences in densities, refractive indexes, and sizes of the droplets and bubbles make the analysis of these two materials as mixtures almost impossible.

In the current work, we aimed to study PDA-coated, PFH-containing emulsions (or PDA/PFH emulsion droplets) as the model emulsion system using small- and ultra-small-angle neutron scattering (SANS and USANS, respectively). SANS and USANS are ideal for characterising these emulsion systems and monitoring their phase transition into microbubbles. The combination of these techniques grants access to a combined length-scale ranging from 1.0 nm to 10 microns, appropriate for colloidal systems in the nano-, meso-, and microscale regime. These techniques have been applied to a variety of emulsion systems,[25-27] but rarely to microbubbles. Herein, we utilised SANS and USANS, employing contrast variation and a temperature-controlled sample tumbling system, to observe the temperature-triggered phase change of PDA/PFH emulsion droplets and explore changes in the structural properties of these colloids. This setup is ideal for metastable samples, such as PDA/PFH emulsions, that require constant mixing during neutron scattering analysis. Use of this setup addresses the problems introduced by mismatched density, ensuring that data obtained from analyses represent the total population within the sample.

2 Results and discussion

2.1 Morphological characterisation of the PDA/PFH emulsion droplets

In the current work, we fabricated and characterise PDA/PFH emulsion systems. Oxidative polymerisation of dopamine with the PFH pre-emulsion, obtained by sonication with Pluronic F-127 and copper sulphate solution at high pH (8.4), yields mixtures with dark brown to black colour (**Fig. S1A and S1B**), which is a characteristic of PDA.[4] As shown in dynamic light scattering (DLS) data, the effective diameters of these emulsion droplets are around 600 nm with size distributions ranging from around 100 nm to about 6 µm (**Fig. S1C**), which was also observed in optical microscopy images (**Fig. S1D**). To visualise the submicron-sized droplets, samples were imaged using transmission electron microscopy (TEM). TEM images, in **Figure 1D**, showed that the droplets with 200 nm to 600 nm diameters with the smooth PDA coating. TEM images of some droplets, fixed in 90-nm resin slices, revealed that the droplets have 200 nm to 600 nm diameters and that the PDA shell of these droplets is about 10–20 nm in thickness (**Figure S1A**). The main differences between the morphologies of 2H and 4H are the slightly larger sizes and less uniform shell thickness in the former, compared to the latter. We hypothesized that these dissimilarities could result in differences in the phase transition of these two samples during heating.

Our initial attempts to trigger the phase transition of these droplets into microbubbles by heating gave inconsistent and conflicting results due to a number of limitations of DLS and other the available techniques. The main problem with utilising DLS in observing phase change emulsion droplets is the density difference between the emulsion and the microbubbles, leading to droplet sedimentation at bottom of the tube, and microbubbles rising towards the liquid surface.

2.2 Neutron scattering setup and contrast matching

In this current work, we utilised SANS and USANS, employing contrast variation and a temperature-controlled sample tumbling system, to observe the temperature-triggered phase change of PDA/PFH emulsion droplets and explore changes in the structural properties of these colloids. The Sample Environment team within the Australian Centre for Neutron Scattering at ANSTO developed the tumbling system, composed of multiple rotating sample holders, with a circulating bath for temperature control. This setup is ideal for metastable samples, such as PDA/PFH emulsions, that require constant mixing during neutron scattering analysis. Use of this setup addresses the problems introduced by mismatched density, ensuring that data obtained from analyses represent the total population within the sample.

One important advantage of neutron scattering techniques that we highlight in this work is the opportunity for contrast variation. In order to obtain scattering information from the emulsion droplets and the microbubbles separately, mixtures with different mass ratios of water (H_2O) and deuterium oxide (D_2O) were utilised as dispersing media to match the scattering length densities (SLD) of these colloidal species (**Fig. 1A**). A 9:91 D_2O:H_2O mixture (SLD ≈ 0.00 $Å^{-2}$) was used to match out the scattering from microbubbles (SLD = 2.6×10^{-8} $Å^{-2}$) and highlight the neutron scattering from the emulsion droplets (SLD = 3.5×10^{-6} $Å^{-2}$). Likewise, scattering from microbubbles was highlighted by matching out scattering from the emulsion droplets, using a 61:39 D_2O:H_2O mixture (SLD = 3.5×10^{-6} $Å^{-2}$). **Figure 1B** shows the stitched (combined) SANS and USANS patterns of PDA/PFH emulsion droplets, demonstrating the capability of these two techniques in reproducibly probing a wide length-scale, suitable for characterisation these materials. PDA (SLD = 1.6×10^{-6} $Å^{-2}$) and Pluronic F-127 should have negligible contribution to the overall scattering due to their very small amounts (0.03% by weight) in the emulsion samples, in comparison with the bubbles and droplets. Hence, the SLDs of these materials were not accounted in the contrast matching.

2.3 Monitoring microbubble production and droplet depletion

Fig. 2A and 2B show the USANS patterns of PDA/PFH droplets with polymerisation times of two and four hours (2H and 4H, respectively) in droplet-matched continuous phase from 20°C to 90°C. USANS is an excellent technique for observing microbubble formation as it can probe samples with size ranges that fall in the meso- and microscale region (~100 nm to 10 µm). Both samples had low scattering intensities at low temperatures, since the microbubbles are ideally non-existent before heating, and the scattering from the emulsion droplets is contrast matched out. Small fluctuations in scattering intensity between 22°C to 46°C, however, may indicate that small quantities of microbubbles were already present in the 4H sample, due to the fabrication process. Increases in scattering intensities, denoting microbubble formation, in the low-q region (~3.7×10^{-5}–1.0×10^{-5} $Å^{-1}$) were only observed in sample 2H starting at 50°C with maximum intensity at around 74–78°C. For sample 4H, the scattering intensities in the low-q region (~5.3×10^{-5}–7.0×10^{-5} $Å^{-1}$) started to increase at around 70°C with maximum intensity at 90°C.

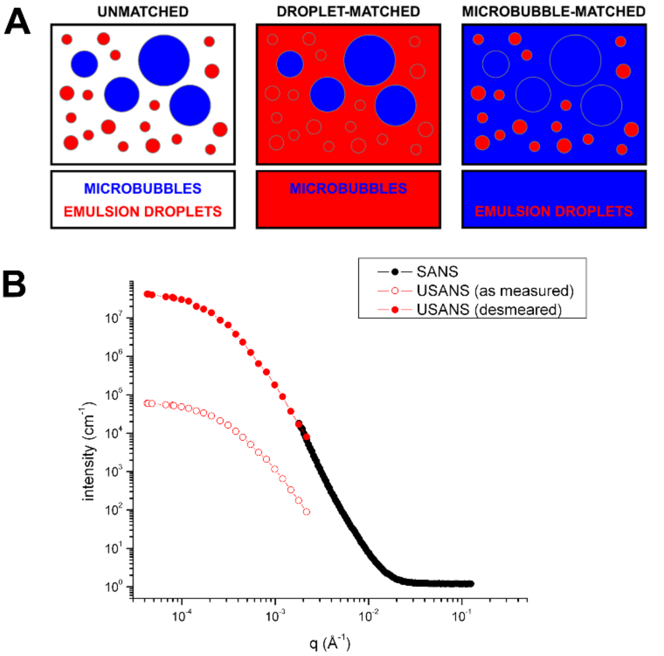

Figure 2. (**A**) A cartoon depicting obtained contrast conditions of the mixtures containing the emulsion droplets and microbubbles. An **unmatched** dispersing medium does not match the scattering length densities of either the bubbles or the droplets; hence, the scattering observed is a mixture from both colloidal species. The **droplet-matched** medium highlights the neutron scattering from the microbubbles while the **bubble-matched** medium highlights the scattering from the emulsion droplets. (**B**) A plot showing the stitched SANS and USANS spectra of PDA/PFH emulsion droplets. SANS data are represented by the black-filled circles, while USANS data are represented by the red circles: unfilled – prior to desmearing; and red-filled – desmeared data.

These observed phase transition temperatures of 2H and 4H are much higher than the bulk boiling point of PFH (56°C). The discrepancies between the observed boiling points of the samples and expected boiling point of PFH could be an effect of the small size of the PFH droplets, which effected increased Laplace pressure, and also by the presence of other emulsion components (PDA and surfactant), which delayed the onset of boiling.[20, 28-30] To a crude first approximation (*i.e.* discounting the effects of shell composition), this increase can be predicted using the Clausius–Clapeyron equation. Assuming a water–PFH interfacial tension of 56 mN m^{-1},[31] for a 1-µm radius droplet of PFH (heat of vaporisation, $\Delta_{vap}H^{o}$ = 32.4 kJ mol^{-1} from the NIST database[32]) the anticipated boiling point is 83°C, compared to 60°C for bulk liquid PFH. These simple calculations show good agreement with observed effects, indicating that confinement in droplets is the primary cause of boiling point increase for these emulsified fluorocarbons. The slight decrease in the USANS intensities from the emulsion droplets at the upper temperature range used, as shown in **Fig. 2C and 2D**, for 2H and 4H, respectively, supports the idea that the samples have only started to boil at these temperatures. Furthermore, these observations indicate that there is no significant decrease in the droplets within 500 nm to 10 µm.

In order to get more information about changes in the emulsion droplets, we observed the SANS intensities of the same samples at different temperatures to access a probed lengthscale of about 1 nm to 500 nm. As shown in **Fig. 2E and 2F**, scattering intensities of 2H and 4H, respectively, both decreased significantly with increasing temperature until a constant value was reached, denoting that no further droplets within this size range are lost. For 2H, a constant, low intensity was reached at around 60°C at q = 0.0034 Å^{-1} (**Fig. 2G**), while for 4H, a low intensity was reached at around 70°C at the same q value (**Fig. 2H**). These results complement the findings of USANS – the earlier phase transition of 2H and delayed phase transition of 4H. SANS patterns of microbubbles from the droplet-matched mixture showed very low intensities as the lengthscale of these materials are outside the SANS region; hence, these were not used in any data analysis.

The observed intensity changes in SANS indicate that smaller emulsion droplets (**Fig. 3A** and **3B**, **Fig. S2A**–**S2B**) are destroyed first at lower temperatures. The slight drop in the USANS intensities at around 70–90°C indicate that larger droplets only start to disappear at higher temperature. Expansion of droplets at slightly elevated temperatures (between 40 and 50°C) may also damage the PDA shell without the liquid PFH core transitioning into gas bubbles, as shown in the TEM image in **Fig. S2C**. This can give an opportunity for these small droplets to coalesce and form micron-sized droplets, which might have contributed to the observed stable values of the scattering intensities of the droplets in USANS. We believe that these larger droplets are Pickering emulsions, similar to some reports in literature,[33-35] which are stabilised by loosely bound, collapsed PDA shells (**Fig. 3C**–**3F**, **Fig. S2D and S2E**).

2.4 Evaluation of droplet size and structures

To study temperature-dependent structural changes of the emulsions, USANS patterns were obtained before heating the samples at 20°C, at 90°C, and after cooling down the mixtures to 20°C (**Fig. S3**). The USANS scattering patterns of the 2H and 4H emulsion droplets show one broad Guinier feature, in agreement with the expected spherical fluorocarbon droplets with some polydispersity. These data could be fitted reasonably well with a Guinier-Porod model, which yielded radii of gyration (Rg) and Porod exponents (Table 1). Assuming spherical droplets of uniform scattering density and using $R_g = R\,(3/5)^{1/2}$,[36] the associated droplet radii R were also calculated.

The emulsion droplets from 2H had an average droplet radius of 842 nm at 20°C, which increased to 886 nm upon heating to 90°C. After cooling back to 20°C, the remaining droplets showed a droplet radius of 872 nm. These results indicate that 2H droplets only experienced minimal changes in structure at different temperatures. Meanwhile, the emulsion droplets from 4H had a droplet radius of 870 nm at 20°C. At 90°C where phase change had already occurred, the emulsion droplets showed an average radius of 949 nm. After cooling down to 20°C, the average radius of remaining droplets (R = 1008 nm) was even higher than that at 90°C. This significant change in droplet radii may indicate that sample 4H was less stable compared to sample 2H. This observation may also confirm either or both the coalescence of PFH droplets and recondensation of vapourised PFH contributed to the increase in droplet radius of sample 4H, which we believe existed as a Pickering emulsion (**Fig. 3C** and **3D**). DLS results at 25°C (**Fig. 1**) showed very different results from the calculated radii from the USANS patterns, which could be attributed to quick settling of large droplets due the static conditions of the samples in DLS. Because of the sample polydispersity, size estimation for the smaller droplets was not possible; however, all SANS curves of the bubble-matched samples showed Porod exponents of 4.00 ± 0.03 (**Table S1**), confirming that the emulsion droplets with diameters below 500 nm are very smooth and show a sharp interface.

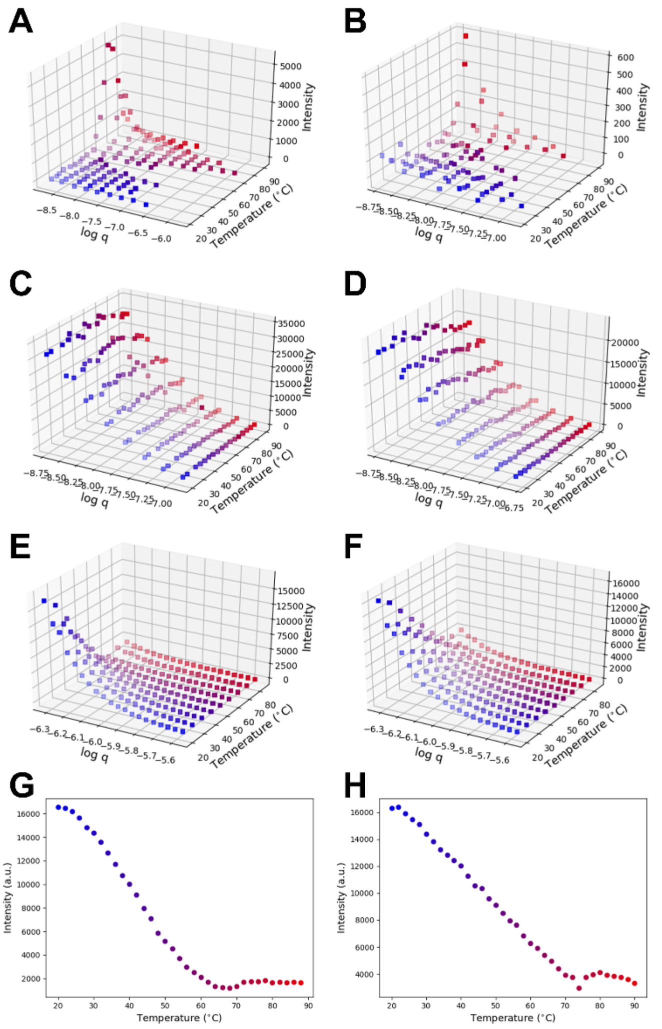

Figure 3. Three-dimensional plots showing the: USANS spectra of droplet-matched (**A**) 2H and (**B**) 4H dispersions; USANS spectra of bubble-matched (**C**) 2H and (**D**) 4H dispersions; and SANS spectra of droplet-matched (**E**) 2H and (**F**) 4H dispersions at different temperatures. SANS intensities of bubble-matched (**G**) 2H and (**H**) 4H dispersions from 20°C to 90°C, at q = 0.0034 Å^{-1}. Scattering intensities in droplet-matched (61% D_2O/ 39% H_2O) and in bubble-matched (9% D_2O/ 91% H_2O) samples arise from microbubbles and emulsion droplets, respectively. 2D plots are shown in the Supporting Information (**Fig. S3** and **S4**).

Table 1. Properties of PDA/PFH emulsions, calculated from USANS data at different temperatures.

Parameter	**Sample 2H**			**Sample 4H**		
	20°C (start)	*90°C*	*20°C (cooled)*	*20°C (start)*	*90°C*	*20°C (cooled)*
Radius of gyration (nm)	652 ± 4	686 ± 5	675 ± 5	674 ± 5	735 ± 6	781 ± 6
Radius (nm)	842 ± 5	886 ± 6	872 ± 7	870 ± 7	949 ± 7	1008 ± 8
Porod exponent	3.23 ± 0.03	3.39 ± 0.05	3.20 ± 0.04	2.99 ± 0.04	3.50 ± 0.05	3.45 ± 0.05

Interfacial structures of the microbubbles were also studied by fitting USANS and SANS patterns of the droplet-matched mixtures to a simple power-law fit. As shown in **Fig. S3**, the scattering from the microbubbles in both samples started with very low signal at 20°C. At 90°C, the scattering patterns of samples 2H and 4H are steep curves with Porod exponents of 3.51 and 3.43, respectively, clearly showing the production of microbubbles. These Porod exponents indicate that bubbles formed have some degree of roughness, which is attributable to broken droplet shells and remaining droplets that may adsorb at the droplet interface. Unfortunately, the absence of scattering in the Guinier region in USANS plots indicates that the size of formed bubbles are outside the *q* range of USANS; hence, average bubble diameters are beyond 10 µm and the exact sizes cannot be estimated.

Despite the demonstrated potential of the techniques and setup used in this work, there are still challenges and limitations that need to be addressed. While structures can be identified, getting the average size of the droplets or the microbubbles can be difficult especially when their size changes extend beyond the limits of the *q* range of USANS. This means that, in order to have a complete view of the process, other imaging and scattering techniques would still be required to complement the results that can be obtained from these neutron experiments. Furthermore, many colloidal materials that are being developed for various applications exhibit a certain degree of polydispersity. This presents another layer of complexity in analysis and model fitting, but these are important to explore since many natural and artificial colloids and assemblies exhibit this heterogeneity. Finally, we predict that the setup and method used here can be applied to study contrast agents in more complex mixtures in order to simulate real life systems (such as salt and buffer mixtures, protein-containing dispersants) but this would require intricate contrast matching experiments.

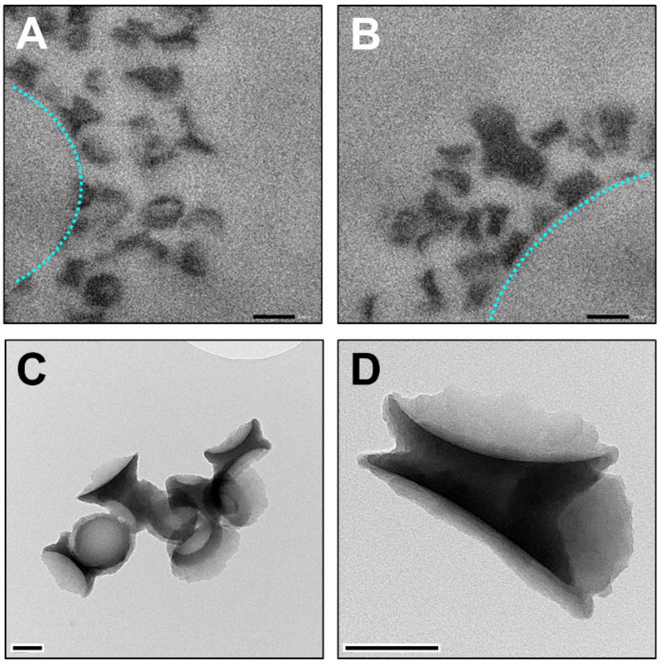

Figure 4. Representative transmission electron micrographs. (A and B) Collapsed PDA shells surrounding curved regions that are potentially interfaces of pre-existent emulsions or bubbles. Blue dotted lines are the interfaces of the colloidal materials. (C and D) Collapsed, dried PDA shells of PDA/PFH emulsion droplets. Scale bars = 100.

3 Experimental

3.1 Materials and reagents

Dopamine hydrochloride ($C_8H_{11}NO_7$ HCl, Sigma-Aldrich), copper sulfate pentahydrate ($CuSO_4{\cdot}5H_2O$, Sigma-Aldrich) and Pluronic F-127 (Sigma-Aldrich), tris(hydroxymethyl)-aminomethane hydrochloride (TRIS HCl, ultrapure, VWR Life Science), UltraPure^{TM} Agarose (Invitrogen, Thermo Fisher Scientific) and perfluorohexane (C_6F_{14}, FluoroChem) were used as received.

3.2 Preparation of polydopamine-coated perfluorohexane (PDA/PFH) emulsion droplets[4]

A mixture, containing 14.00 mL Tris buffer (10 mol L^{-1}, pH 8.5), 5.0 mg Pluronic F-127, 250.0 µL perfluorohexane, and 130.0 µL $CuSO_4$ solution (40.0 mg mL^{-1}), was prepared in a 25 mL glass vial at room temperature. A 3.175-mm ultrasonicator microtip (Consonic) was submerged in the solution and positioned right above the level of the PFH. Right before sonication, a freshly prepared mixture of 1.0 mL Tris buffer (10 mol L^{-1}, pH 8.5) and 5.0 mg dopamine hydrochloride was added to the suspension. The suspension, submerged in an ice bath, was then sonicated using a Branson Digital Sonifier SFX 550 (Emerson Electric Co.) for 120 s at 10% amplitude (power output = 3 W) to yield the emulsion droplets. The uncapped vial was removed from the ice bath and then stirred for five hours. Every hour, two 1.50 mL portions of the emulsion were taken from the mixture, and then washed twice by centrifugation at 4000 ×g for one minute, followed by re-dispersion in 1.00 mL water to remove the unreacted dopamine hydrochloride and excess Tris buffer. The washed, concentrated emulsions were refrigerated at 4°C until further use. Each concentrated emulsion from 1.50 mL of the original mixture was redispersed in 1.50 mL D_2O-H_2O mixtures, having final mass ratios of 61:39 and 9:91, to match the SLDs of the liquid PFH emulsion droplets (SLD = 3.5×10^{-6} Å^{-2}) and of the PFH microbubbles (SLD = 2.6×10^{-8} Å^{-2}), respectively.

3.3 Dynamic light scattering analysis

Effective diameters of the emulsion droplets were determined by dynamic light scattering (DLS), using a Brookhaven NanoBrook Omni particle sizer and zeta potential analyser. Samples were also visualised by optical microscopy.

3.4 Analysis of PDA shell size and morphology by transmission electron microscopy

Emulsion samples (10 µL) were pipetted onto a parafilm-covered glass plate. Carbon-coated 300 mesh copper grids were incubated for five minutes on top of the emulsion droplets with the carbon face down. Following incubation, the excess emulsion sample was blotted away with filter paper and the grids were placed face down onto 10 uL droplets of 1% aqueous uranyl acetate. The grids were incubated on uranyl acetate for 30 seconds, after which the uranyl acetate was blotted away with filter paper and the grids allowed to dry. Negatively stained emulsion droplets on the TEM grids were imaged in a JEOL JEM-1400 Plus transmission electron microscope (JEOL USA, Inc.) with an accelerating voltage of 80 keV and a spot size 2. Digital images were captured with a resolution of 2048 x 2048 pixels.

Size and morphology of the collapsed PDA shells were also studied using transmission electron microscopy (FEI Tecnai T20 TEM) at 200 keV. Samples were prepared by drop casting 3.0 µL aliquots of the droplet dispersions onto holey carbon film-coated, 300 mesh copper grids (EM Solutions), which were then air dried overnight, prior to analysis.

To get a clear image of the PDA shell thickness, ultramicrotomed resin slices, containing the emulsion droplets were imaged. Briefly, concentrated emulsions were dispersed in melted 4% agarose at 40°C, which was then cooled and transferred into a mixture of Epon resin. The resin, containing the fixed emulsions, were then sectioned into 90-nm slices with a diatome diamond knife using a Leica EM UC7 ultramicrotome (Leica Microsystems). Slices were loaded onto formvar-coated, 100 mesh copper grids and then imaged using a JEOL JEM-1400plus TEM (JEOL USA, Inc.) at 80 keV.

3.5 Small-angle neutron scattering (SANS) and ultra-small-angle neutron scattering (USANS)

SANS and USANS experiments were performed respectively using the Bilby[37] and Kookaburra[38] beam-lines at the Australian Centre for Neutron Scattering, Australian Nuclear Science and Technology Organisation (ANSTO), Lucas Heights, Australia. Samples dispersions (1.2 mL) were loaded into 1.5-mL aluminium sample cells with quartz windows (40 mm diameter x 1 mm thick), leaving an approximately 3.0 mL free volume for gas expansion during heating in the SANS and USANS experiments. The cells were mounted into a temperature controlled, six-position sample tumbler, with an aluminium shroud, where silicon glass plates cover the sample cells. All neutron scattering measurements were carried out at a bath temperature range of 20°C to 90°C, while tumbling with at least 30 minutes equilibration at each temperature tested. For SANS and USANS measurements, a 17.5-mm borated aluminium aperture and a 12.5-mm Cd aperture, respectively, was positioned at the centre of the filled space of the cell to avoid the neutron beam from hitting the unfilled part of the cell.

SANS measurements were carried out in velocity selector mode with the incident neutron wavelength set at 11 Å. The raw scattering counts were collected on the main detector at a sample-detector distance of 18 m, combined with four curtain detectors at 1.8 and 2.8 m. The data were reduced using the Mantid[39] package, resulting in radially averaged intensity data I(q) where the scattering vector q is defined as:

$$q = \frac{4\pi}{\lambda} sin \frac{\theta}{2}$$

with λ the incident neutron wavelength and θ the scattering angle. Absolute intensity scaling was achieved based on an empty beam transmission measurement, and the simultaneous q range was 0.0017–0.2 Å^{-1}. For background subtraction, an empty cell measurement was used.

Kookaburra is a USANS instrument, based on the classical Bonse-Hart method, where the monochromator and analyser consist of two identical arrays of five-reflection, channel-cut silicon single crystals, aligned in a non-dispersive, parallel geometry that produces Bragg reflection conditions. An incident neutron wavelength of 4.74 Å was used. Rocking curve profiles were obtained by rotating the analyser crystal away from the aligned peak position and measuring the neutron intensity as a function of the scattering vector q, point by point. The total q range was 0.00003–0.01 Å-^{1}, however the highest q-value is often limited by reduced signal-to-noise ratio, due to time constraints in kinetic experiments. Data were reduced by using Python scripts in Gumtree,[40] based on the standard procedure.[6] Data for Figure 1B were desmeared using IgorPro software with the NIST Macro for USANS reduction.[41]

It is important to note that Bilby SANS is ideal for kinetic measurements, because it collects the whole q range at once, while Kookaburra USANS performs the measurements point by point, where the points with low intensities (typically at high q) may take up to 20 minutes each to get good statistics. Hence, USANS curves for each temperature are usually of low resolution (lower number of points), because these measurements typically take significantly longer times than Bilby SANS. One of the advantages of Kookaburra USANS is its lower q range than SANS that allows probing of structures with bigger lengthscales (100 nm to 10 µm).

3.6 Data Analysis

USANS data were fitted to models using SasView software (https://www.sasview.org). A Guinier-Porod model was used to fit the USANS data for samples scanned in 9% D_2O (bubble-matched). Since the Guinier region was beyond the q range of the bubbles, data obtained from samples in a 61% D_2O (droplet-matched) were fitted using a power-law model.

4 Conclusions

We have demonstrated that the tandem techniques of SANS and USANS, combined with contrast matching, temperature control and tumbling systems, can be applied in monitoring real-time changes in the population of a model phase change emulsion system and the microbubbles generated. Furthermore, results of SANS and USANS analyses indicate that smaller droplets are destroyed first at lower temperatures, while larger droplets disappear at higher temperatures. A reasonable interpretation of this is that smaller droplets are destabilised at elevated temperatures and undergo coalescence. Meanwhile, larger droplets transition into microbubbles, but only to a minimal extent due to the increased boiling points of these systems, as an effect of size reduction.[42] However, this logical assumption still needs further validation. Information obtained from these studies could be valuable in predicting and explaining thermal responsiveness and stability of these perfluorocarbon emulsion systems, and can complement other characterisation and visualisation techniques. To the best of our knowledge, this is the first report on the application of SANS and USANS in observing *in situ* phase transitions of liquid emulsions into microbubbles upon application of heat. With the method described in this work, we anticipate that the application of these techniques can be extended to other unstable and dynamic colloidal systems.

Author Contributions

Mark Louis P. Vidallon: Conceptualisation, Methodology, Investigation, Visualisation, Writing – Original draft. **Luke W. Giles:** Visualisation, Writing – Review & Editing. **Simon A. Crawford:** Investigation. **Alexis I. Bishop:** Resources, Supervision, Writing – Review & Editing. **Rico F. Tabor:** Resources, Supervision, Funding acquisition, Writing – Review & Editing. **Liliana de Campo:** Methodology, Validation, Investigation, Formal analysis, Supervision, Project administration, Writing – Review & Editing. **Boon Mian Teo:** Conceptualisation, Methodology, Investigation, Resources, Supervision, Project administration, Funding acquisition, Writing – Review & Editing.

Conflicts of interest

There are no conflicts to declare.

Acknowledgements

The authors acknowledge the support of the Australian Nuclear Science and Technology Organisation (ANSTO), in providing the Bilby SANS and Kookaburra USANS instruments and facilities used in this work. We also acknowledge the use of instruments and assistance at the Monash Centre for Electron Microscopy (MCEM) and Ramaciotti Centre for Cryo-Electron Microscopy, Nodes of Microscopy Australia. This work benefited from the use of the SasView application, originally developed under NSF award DMR-0520547. SasView contains code developed with funding from the European Union's Horizon 2020 research and innovation programme under the SINE2020 project, grant agreement No 654000. M.L.P.V. and L.W.G. would like to thank AINSE Limited for providing financial assistance though AINSE PGRA to enable work on ANSTO beamline facilities. Monash University, Faculty of Science Dean's Postgraduate Research Scholarship (M.L.P.V.) and the Australian Government Research Training Program (RTP) Scholarship (L.W.G) support this research.

References

1. M. Ghorbani, K. Olofsson, J.-W. Benjamins, K. Loskutova, T. Paulraj, M. Wiklund, D. Grishenkov and A. J. Svagan, *Langmuir*, 2019, **35**, 13090-13099.
2. J. Y. Lee, C. Crake, B. Teo, D. Carugo, M. de Saint Victor, A. Seth and E. Stride, *Advanced Healthcare Materials*, 2017, **6**, 1601246.
3. A. Ishijima, J. Tanaka, T. Azuma, K. Minamihata, S. Yamaguchi, E. Kobayashi, T. Nagamune and I. Sakuma, *Ultrasonics*, 2016, **69**, 97-105.
4. C. Mannaris, C. Yang, D. Carugo, J. Owen, J. Y. Lee, S. Nwokeoha, A. Seth and B. M. Teo, *Ultrason. Sonochem.*, 2020, **60**, 104782.
5. Q. Chen, J. Yu and K. Kim, *Biomedical Engineering Letters*, 2018, **8**, 223-229.
6. C. Mannaris, L. Bau, M. Grundy, M. Gray, H. Lea-Banks, A. Seth, B. Teo, R. Carlisle, E. Stride and C. C. Coussios, *Ultrasound in Medicine & Biology*, 2019, **45**, 954-967.
7. J. Y. Lee, D. Carugo, C. Crake, J. Owen, M. de Saint Victor, A. Seth, C. Coussios and E. Stride, *Adv. Mater.*, 2015, **27**, 5484-5492.
8. C. Mou, Y. Yang, Y. Bai, P. Yuan, Y. Wang and L. Zhang, *Journal of Materials Chemistry B*, 2019, **7**, 1246-1257.
9. J. Zhuang, M. Ying, K. Spiekermann, M. Holay, Y. Zhang, F. Chen, H. Gong, J. H. Lee, W. Gao, R. H. Fang and L. Zhang, *Adv. Mater.*, 2018, **30**, 1804693.
10. J. Zhu, Z. Wang, X. Xu, M. Xu, X. Yang, C. Zhang, J. Liu, F. Zhang, X. Shuai, W. Wang and Z. Cao, *Molecular Pharmaceutics*, 2020, **17**, 817-826.
11. P. S. Sheeran, V. P. Wong, S. Luois, R. J. McFarland, W. D. Ross, S. Feingold, T. O. Matsunaga and P. A. Dayton, *Ultrasound in Medicine & Biology*, 2011, **37**, 1518-1530.
12. S. Guo, X. Guo, X. Wang, D. Zhou, X. Du, M. Han, Y. Zong and M. Wan, *Ultrason. Sonochem.*, 2019, **54**, 183-191.
13. A. S. Hannah, D. VanderLaan, Y.-S. Chen and S. Y. Emelianov, *Biomed Opt Express*, 2014, **5**, 3042-3052.
14. K. Wilson, K. Homan and S. Emelianov, *Nature Communications*, 2012, **3**, 618.
15. J. H. Ryu, P. B. Messersmith and H. Lee, *ACS Applied Materials & Interfaces*, 2018, **10**, 7523-7540.

16. Y.-J. Ho, C.-C. Wu, Z.-H. Hsieh, C.-H. Fan and C.-K. Yeh, *J. Controlled Release*, 2018, **291**, 26-36.
17. E. Strohm, M. Rui, I. Gorelikov, N. Matsuura and M. Kolios, *Biomed Opt Express*, 2011, **2**, 1432-1442.
18. Z. Lu, A. J. Quek, S. P. Meaney, R. F. Tabor, B. Follink and B. M. Teo, *ACS Applied Bio Materials*, 2020, **3**, 5880-5886.
19. E. Strohm, I. Gorelikov, N. Matsuura and M. Kolios, *Journal of Biomedical Optics*, 2012, **17**, 096016.
20. P. S. Sheeran and P. A. Dayton, *Scientifica*, 2014, **2014**, 579684.
21. S. Li, S. Lin, Y. Cheng, T. O. Matsunaga, R. J. Eckersley and M.-X. Tang, *Ultrasound in Medicine and Biology*, 2015, **41**, 1422-1431.
22. Z. Z. Wong, O. D. Kripfgans, A. Qamar, J. B. Fowlkes and J. L. Bull, *Soft Matter*, 2011, **7**, 4009-4016.
23. P. S. Sheeran, S. Luois, P. A. Dayton and T. O. Matsunaga, *Langmuir*, 2011, **27**, 10412-10420.
24. S. Pu, C. Gong and A. W. Robertson, *Royal Society Open Science*, 2020, **7**, 191204.
25. L. Cheng, A. Ye, Y. Hemar, E. P. Gilbert, L. de Campo, A. E. Whitten and H. Singh, *Langmuir*, 2019, **35**, 12017-12027.
26. G. Alvarez, J. Jestin, J. F. Argillier and D. Langevin, *Langmuir*, 2009, **25**, 3985-3990.
27. C. Washington, S. M. King and R. K. Heenan, *The Journal of Physical Chemistry*, 1996, **100**, 7603-7609.
28. N. Rapoport, *WIREs Nanomedicine and Nanobiotechnology*, 2012, **4**, 492-510.
29. N. V. Bulanov and B. M. Gasanov, *Int. J. Heat Mass Transfer*, 2008, **51**, 1628-1632.
30. N. V. Bulanov and B. M. Gasanov, *Journal of Engineering Physics and Thermophysics*, 2006, **79**, 1130-1133.
31. N. Nishikido, W. Mahler and P. Mukerjee, *Langmuir*, 1989, **5**, 227-229.
32. T. Boublík, V. Fried and E. Hála, *The vapour pressures of pure substances : selected values of the temperature dependence of the vapour pressures of some pure substances in the normal and low pressure region*, Elsevier : Distributors for the United States and Canada : Elsevier Science Pub. Co., Amsterdam; New York, 1984.
33. T. Ding, L. Wang, J. Zhang, Y. Xing and K. Cai, *Journal of Materials Chemistry B*, 2018, **6**, 1754-1763.
34. N. Nishizawa, A. Kawamura, M. Kohri, Y. Nakamura and S. Fujii, *Polymers (Basel)*, 2016, **8**, 62.
35. J. Xu, A. Ma, T. Liu, C. Lu, D. Wang and H. Xu, *Chem. Commun.*, 2013, **49**, 10871-10873.
36. B. Hammouda, *J. Appl. Crystallogr.*, 2010, **43**, 716-719.
37. A. Sokolova, A. E. Whitten, L. de Campo, J. Christoforidis, A. Eltobaji, J. Barnes, F. Darmann and A. Berry, *J. Appl. Crystallogr.*, 2019, **52**, 1-12.
38. C. Rehm, L. de Campo, A. Brule, F. Darmann, F. Bartsch and A. Berry, *J. Appl. Crystallogr.*, 2018, **51**, 1-8.
39. O. Arnold, J. C. Bilheux, J. M. Borreguero, A. Buts, S. I. Campbell, L. Chapon, M. Doucet, N. Draper, R. Ferraz Leal, M. A. Gigg, V. E. Lynch, A. Markvardsen, D. J. Mikkelson, R. L. Mikkelson, R. Miller, K. Palmen, P. Parker, G. Passos, T. G. Perring, P. F. Peterson, S. Ren, M. A. Reuter, A. T. Savici, J. W. Taylor, R. J. Taylor, R. Tolchenov, W. Zhou and J. Zikovsky, *Nuclear Instruments and Methods in Physics Research Section A: Accelerators, Spectrometers, Detectors and Associated Equipment*, 2014, **764**, 156-166.
40. D. M. N. Xiong, T. Lam and N. Hauser, *Journal*, 2017, DOI: 10.5281/zenodo.375967.
41. S. R. Kline, *J. Appl. Crystallogr.*, 2006, **39**, 895-900.
42. X. Xu, R. Song, M. He, C. Peng, M. Yu, Y. Hou, H. Qiu, R. Zou and S. Yao, *Lab on a Chip*, 2017, **17**, 3504-3513.